A twist for tunable electronic and thermal transport properties of nanodevices

Journal:	*Nanoscale*
Manuscript ID	NR-ART-01-2024-000058.R1
Article Type:	Paper
Date Submitted by the Author:	21-Feb-2024
Complete List of Authors:	Ostovan, Azar; UCSB Milowska, Karolina; CIC nanoGUNE Garcia-Cervera, Carlos; UCSB

Nanoscale

ARTICLE TYPE

Cite this: DOI: 00.0000/xxxxxxxxxx

A twist for tunable electronic and thermal transport properties of nanodevices†

Azar Ostovan,*[a] Karolina Z. Milowska,[b,c] and Carlos J. García-Cervera*[a,d]

Received Date
Accepted Date

DOI: 00.0000/xxxxxxxxxx

Twisted graphene-layered materials with nonzero interlayer twist angles (θ) have recently become appealing, as they exhibit a range of attractive physical properties, which include a Mott insulating phase and superconductivity. In this study, we consider nanodevices constructed from zigzag graphene nanoribbons with a top rectangular benzenoid [6,3]-flake. Using density functional theory and a non-equilibrium Green's function approach, we explore how the electronic and thermal transport properties in such nanodevices can be tuned through a twist of the top flake by an angle $0^\circ \leq \theta \leq 8.8^\circ$ for different stacking configurations. We found a strong dependency of the electronic structure on the stacking type, as well as on the twisting regime, specifically in AA-stacking devices. Electron and hole van Hove singularities (vHSs), which originate, respectively, from the flatness of the top of the valence band for the minor-spin component and the bottom of the conduction band for the major-spin component, are found very close to the Fermi level in the density of states and electronic transmission spectra of AA-stacking devices with a twist angle of 1.1°. We establish that these vHSs in AA-1.1° devices are stable at higher temperatures and, with the increased number of available states, lead to larger values of electron thermal conductivity and finally total thermal conductivity in AA-1.1°. Our work highlights the essential role of twisting and stacking for the fabrication of nanoscale charge and heat switches and spurs future studies of twisted layered structures.

1 Introduction

Graphene twistronics, that is, the study of how rotational mismatch between the vertically stacked layers of graphene affects their electronic properties, has opened up a realm of striking quantum phenomena since the discovery of the graphene magic angle.[1–4] The miracle of twistronics has successfully unlocked phenomena such as Mott insulating phase,[5] unconventional superconductivity,[6] and quantized anomalous Hall effect.[7]

In twisted bilayer materials, due to the reduction in the stacking symmetry, the interlayer electrostatic potential varies between twisted layers[8]. As a result, electrons cannot move freely for shallow twisting angles (θ) that are incommensurate with a graphene monolayer.[9] The manipulation of the bilayer symmetry by an angular mismatch results in novel properties, including, but not limited to, spin polarization effects,[10] ferroelectricity,[11] and chiral phonons[12] has shown potential for innovations in the fabrication of novel nanodevices, i.e. spintronics[13], quantum bits,[14] and phononic devices.[15] Theoretically, it has been realized that crossed graphene nano-ribbons (GNRs) with large twisting values and strong suppression of the interlayer interaction, can acquire beam splitters and electron mirrors when integrated into nanodevices.[16–18]

In this study, we investigate both the electronic and thermal conductance in nanodevices composed of a zigzag graphene nano-ribbon (ZGNR) and a twisted rectangular benzenoid [6,3]-flake, where 6 counts the number of hexagons along the zigzag edge and 3 counts the hexagons along the armchair edge. These types of flakes are among one of the smallest hydrocarbon structures to possess an antiferromagnetic ground state similar to ZGNRs[19,20] (see Figure 1(a) for a description of the structure). Our work demonstrates that the ZGNR and twisted top [6,3]-flake junctions in AA-stacking devices provide a way to tune the conductance from a low conductance OFF-state for $\theta \leq 2.2^\circ$ to a high conductance ON-state for $\theta \geq 4.4^\circ$, while the AB-stacking devices remain at the ON-state for all twisting values. Surprisingly, the thermal transport calculations suggested that the twist between the ZGNR and [6,3]-flake could effectively allow us to engineer the heat flow through the AA-devices. The thermal conductivity of AA-stacking is higher for lower twisting angles (1.1°) than for larger twisting values due to a temperature-controlled DOS and the appearance of stable electron and hole van Hove singularities very close to the Fermi level.

---

[a] *Mathematics Department, University of California, Santa Barbara, CA 93106, USA; E-mail:azarostovan@ucsb.edu*
Email:cgarcia@ucsb.edu
[b] *CIC nanoGUNE, Tolosa Hiribidea 76, 20018 Donostia-San Sebastián, Spain*
[c] *Ikerbasque, Basque Foundation for Science, 48013 Bilbao, Spain*
[d] *BCAM, Basque Center for Applied Mathematics, E48009 Bilbao, Basque Country, Spain*

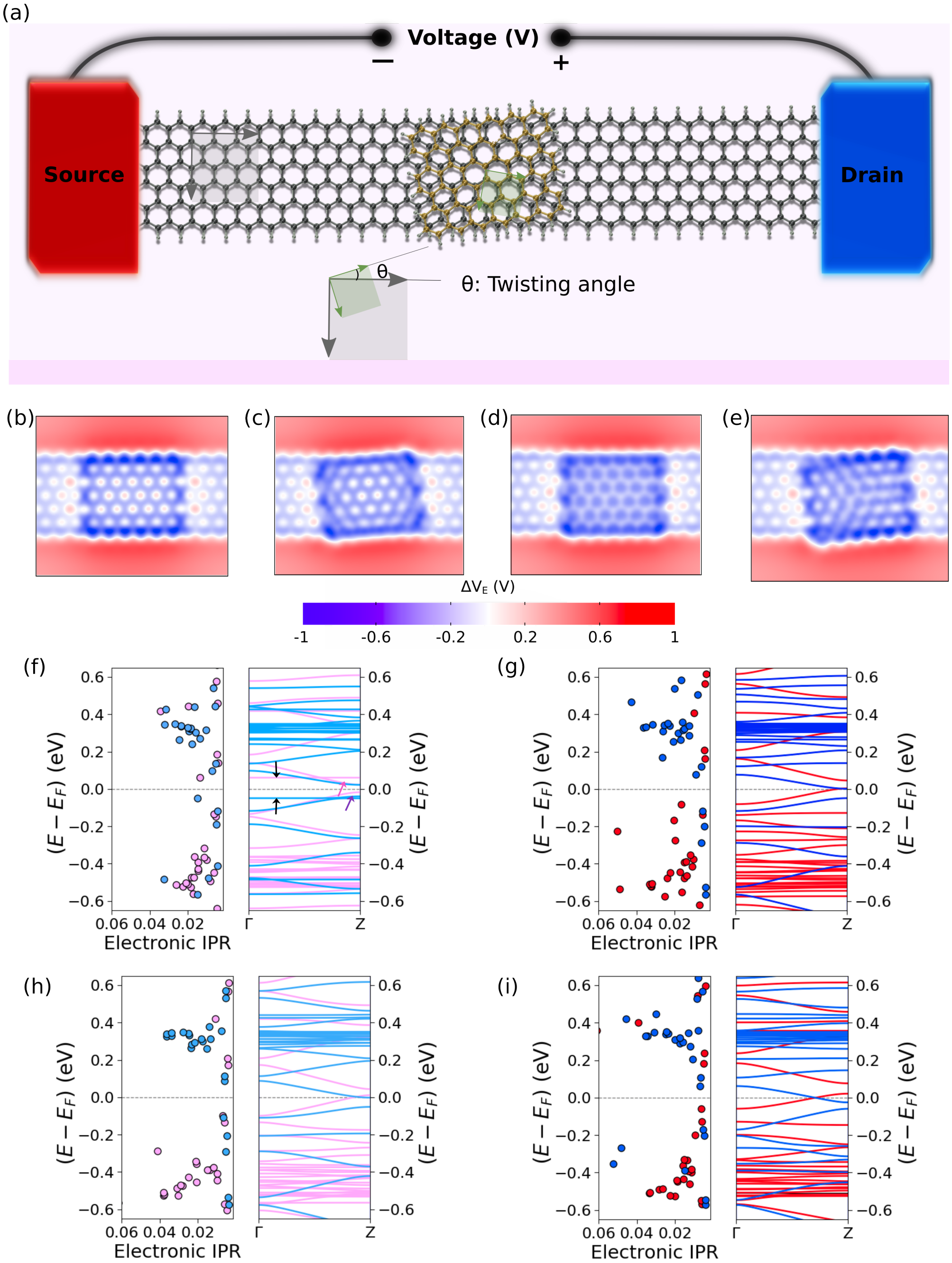

Fig. 1 Device structure and electronic structure analysis of ZGNR controlled by twisted rectangular benzenoid [6,3]-flake. (a) The schematic view of the investigated device. The semi-infinite source and drain electrodes are represented by red and blue cuboids. Interlayer electrostatic potential (in the middle plane between the flake and ZGNR layer) of (b) AA-1.1°, (c) AA-8.8°, (d) AB-1.1°, and (e) AB-1.1°. Spin-resolved electronic inverse participation ratio (IPR) and band structure of (f) AA-1.1°, (g) AA-8.8°, (h) AB-1.1°, and (i) AB-1.1°. The flatness of the top of the CB$^{\uparrow}$ and the bottom of VB$^{\downarrow}$ which gives rise to vHSs very close E_{F} are marked by pink and blue arrows. The flat-band positions associated with VB$-1^{\downarrow}$ and CB$+1^{\uparrow}$, are marked by black arrows. Pink and red colors refer to $IPR^{\uparrow}$ for $\theta = 1.1°$ and $\theta = 8.8°$, respectively. Light and dark blue colors refer to $IPR^{\downarrow}$ for $\theta = 1.1°$ and $\theta = 8.8°$, respectively. Only IPR values above $1/N$ corresponding to the localized states are shown. The interlayer electrostatic potential, inverse participation ratio, and band structure are obtained using DFT/PBE-D2 level of theory.

2 Results

DFT simulations of electronic structure: As a natural starting point we begin by finding the energy difference between the AA and AB-stacking configurations, which can be seen in Figure S1 in the supplemental information (SI). For the bilayer graphene structure (see Figure S1), the AB-stacking is energetically more stable, with an energy that is 0.003 eV/atom lower than the energy of the AA-stacking configuration, which coincides with previously reported computations[21]. As the AA-stacking structure has also been synthesized in experiments[22], in the following we will discuss the properties of both configurations. Also, surprisingly, the calculated energy difference between AA and AB configurations of the nanodevice at $\theta=0^\circ$ (1.8×10^{-3} eV/atom at DFT/vdW-DRSLL and 3×10^{-3} eV/atom at DFT/PBE-D2 levels of theory) indicates that the AA-device is more stable than AB-device (Note S1 (SI)).

The interlayer electrostatic potential of the AA-stacking structures is reduced by the rotation of the top flake. This can be seen in Figure 1(b)-(c), where we plot the electrostatic potential of the AA-stacking structure with a 1.1° rotation (denoted AA-1.1°). Recently it has been reported that the reduction in the stacking symmetry of twisted bilayer ZGNR at $\theta = 90^\circ$ reduces the symmetry of the interlayer electrostatic potential.[23] For AB-stacking structures, there is no obvious variation in electrostatic potential for different twisting values of the top flake (Figure 1(d)-(e)).

The flat-band states (VB$-1^{\downarrow}$ and CB$+1^{\uparrow}$, where VB and CB represent the valence and conduction bands, respectively) are formed in energies very close to the Fermi level for AA-1.1° (Figure 1(f)). The existence of flat bands in twisted bilayer graphene near the magic angle has also been reported in previous computational[24] and experimental studies.[25] The other interesting feature of the band profile is the flatness of the top of the VB and the bottom of CB, which causes the coexistence of electron and hole van Hove singularities (vHs). The associated energy gap (E_g) of 0.0398 eV is calculated between valence and conduction bands of AA-1.1°. The energy gap, nonzero for $\theta = 1.1^\circ$, completely closes at $\theta = 8.8^\circ$ (Table S1). Note that this picture is the same if the flake is placed above the nanoribbon at the optimal distance for AA-8.8° system (3.19 Å) (see Note S3 for details). But in AA-stacking configuration, twisting not only changes their band gap (Figure 1(f)-(g) and Table S1(SI)) but also shifts the Fermi level. The Fermi level goes from being in the gap to being in VB and CB for major and minor-spin components, respectively. This demonstrates that holes are dominant carriers for minor spin-component transport (p-type) while electrons are dominant carriers for major spin-component (n-type) (Figure 1(h)-(i) and Table S1(SI)). The value of E_g was found to be 0.0 eV for AB-stacking, independently of the twisting angle value (Figure 1(h)-(i) and Table S1(SI)). Our results also demonstrated that the nanoflake was edge spin-polarized in both AA and AB configurations. Additionally, the flake edges maintain their spin polarization during twisting, although the difference in spin population between major and minor spin components ($Q_{\uparrow} - Q_{\downarrow}$) may change as the top flake twists (Table S2).

From the local device density of states (LDDOS), one can see that AA-8.8° spin-polarized band states close to E_{F} are located over the bottom layer and the top [6,3]-flake (Figure S3 (c)-(d) (SI)), which means that the states over the top flake can also participate in the carrier transport. The top flake states do not contribute significantly to the LDDOS diagram of AA-1.1°, which implies the top flake states have negligible participation in the charge transport from the first to the second electrode (Figure S3 (a)-(b) (SI)).

To see whether the localization of carriers, especially associated with flat bands, also depends on the twisting angle, we plotted the electronic inverse participation ratio ($IPR^{\uparrow}$ and $IPR^{\downarrow}$, Note S6 (SI)[26]) for bands close to E_{F} (Figure 1(f)-(g), the colored circles). Generally, the $IPR^{\uparrow}$ and $IPR^{\downarrow}$ decrease in value as the twisting angle increases (e.g AA-8.8°), reflecting that these band states are less localized over a larger number of atoms[27]. This also suggests that such devices could potentially be more conductive.[28] On the other hand, the $IPR^{\uparrow}$ and $IPR^{\downarrow}$ for the AB-bilayer somehow show lower variation with rotation (see the colored circles in Figure 1(h)-(i)), which shows that the band probability distribution of AB-structures is less sensitive to twisting.

All the considerations discussed above regarding interlayer electrostatic potential, band structure, LDDOS, and *IPR* demonstrate that, in addition to the stacking formation, the twisting angle between the bottom ZGNR and the top flake affects the electronic structure of ZGNR's bilayer, specially in the case of AA-stacking. This has an effect in the electronic and heat transport of constructed devices and will be discussed in the following sections.

Conductance of ZGNR-twistronics: To capture the dependence of the electronic conductance on the twisting angle, we computed the value of the transmission coefficients for ZGNR-based twistronic devices for AA and AB-stackings as a function of rotational angle ($0^\circ \le \theta \le 8.8^\circ$). The results are shown in Figure 2(a). In Figures S4 and S5 (SI) we also plot the transmission as a function of energy (relative to the Fermi level) for several twisting angles. By placing the rectangular [6,3]-flake on top of the pristine ZGNR layer, the dependence of the transmission coefficients (especially at $E = \pm0.80$ eV) on the twisting angle varies considerably, depending on the stacking type.

The transmission coefficients for the AB-stacking are almost unaffected by the twist, while AA-devices show a significant increase in the transmission values with twisting for $\theta \ge 4.4^\circ$. On the other hand, the transmission values for $\theta = 1.1^\circ$ and 2.2° remain approximately similar to those of the reference system ($\theta = 0^\circ$). This behavior can be observed in the associated conductance plots in Figure S4 (SI) within the energy regions -0.5 < E < -1.5 eV and +0.5 < E < +1.5 eV. The observed conductance dependency of twisted flake and ZGNR on the rotational angle in our investigation differs from the vertical conductivity of the twisted bilayers measured by a tip.[29,30] The vertical conductivity exhibited a nonmonotonic increase for $0^\circ \le \theta \le 5^\circ$ and then it reduces by twisting as a result of suppression of interlayer coupling.

To explain the observed differences, we perform molecular-projected self-consistent Hamiltonian (MPSH)[31] and eigenstate analysis (Figure 2(b) and Figure S6 (SI)). For AA-stacking, at $E = \pm0.8$ eV the hybridization between the $\mathbf{p}_z$ orbitals of the top and bottom layers for rotation angle $0^\circ \le \theta \le 2.2^\circ$ is maximized, leading to a strong electron hopping from the bottom layer to the top flake. For these twistronic devices, the top ribbon plays the role of a trapping site, where electrons will accumulate. This behavior is perfectly reflected in the charge density difference (ΔV_H) profile for AA-1.1° (Figure 2(c)), which clearly shows that there is an interlayer electron transfer from bottom layer to top flake. This causes the top flake to have sites with higher electron concentration, and higher positive values of ΔV_H. On the other hand, for angles $4.4^\circ \le \theta \le 8.8^\circ$, i.e., for higher twisting values, the $\mathbf{p}_z$ orbital hybridization between the carbon atoms is reduced (Figure 2(b)), and electrons can flow from the left to the right electrode, resulting in higher conductance values. The ΔV_H profile of

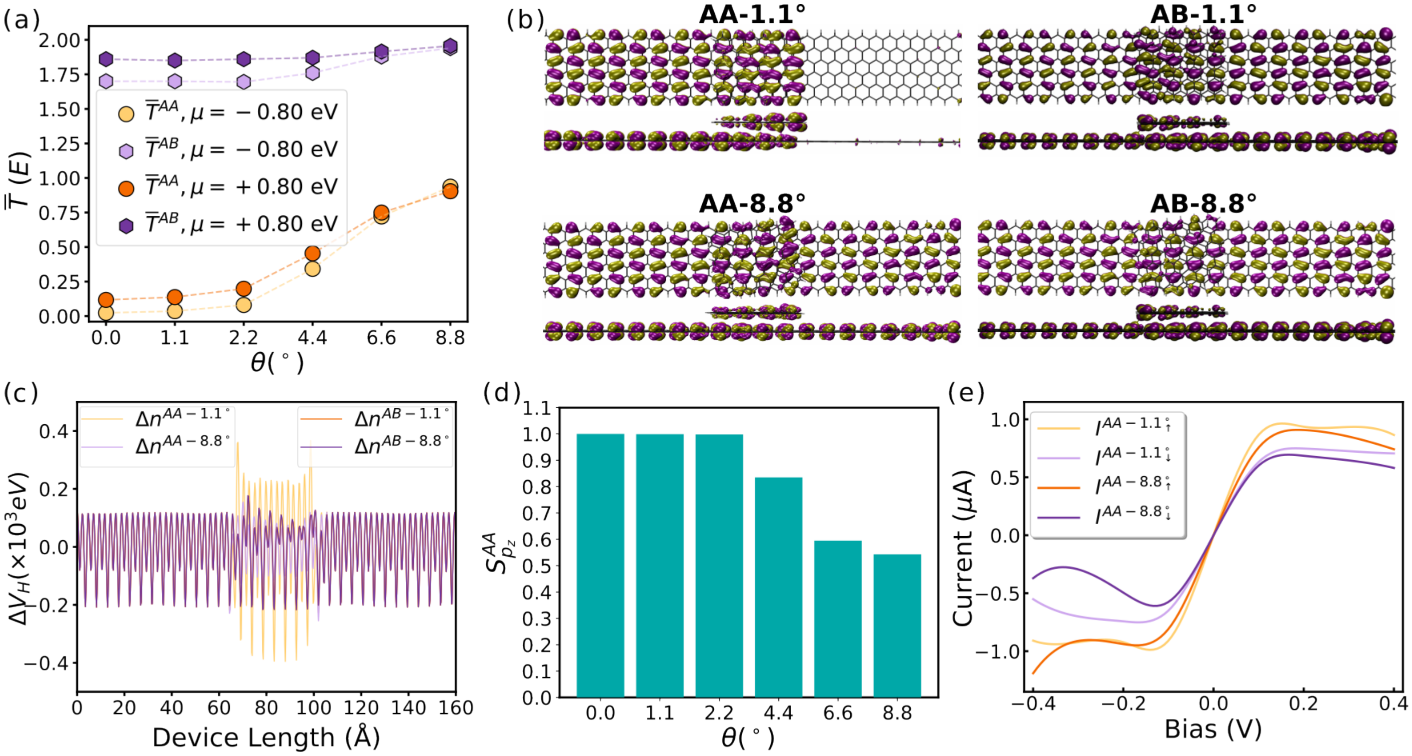

Fig. 2 Obvious difference in electron transport properties controlled by stacking configurations as well as twisting angle. (a) Transmission coefficients ($\overline{T}$ (E)) of AA and AB-stacking nanodevices at two electrochemical potentials ($\mu = \pm 0.8$ eV) as a function of twisting angle (θ). (b) molecular-projected self-consistent Hamiltonian (MPSH) of AA-1.1°, AA-8.8°, AB-1.1°, and AB-1.1° nanodevices at $E = -0.8$ eV. (c) The quantitative charge density plots (ΔV_H) of AA-1.1°, AA-8.8°, AB-1.1°, and AB-1.1° nanodevices projected over the length of device (Å). (d) Normalized overlap integral between $\mathbf{p}_z$ orbitals of top flake and $\mathbf{p}_z$ orbitals of bottom layer for AA-devices ($S_{p_z}^{AA}$) as a function of θ. (e) Calculated spin-resolved current− voltage ($I-V$) characteristics of AA-1.1° and AA-8.8° nanodevices. The transmission coefficients, MPSH, normalized overlap integral between, and current-voltage plots are obtained using DFT/vdW-DRSLL level of theory.

AA-8.8° device is less variant along the transport pathways (Figure 2(c)). The increased conductance values in AB-devices can be explained similarly. When the top flake is shifted to form AB-stacking, the $\mathbf{p}_z$ orbitals of the bilayer central region fall into a hybridization-avoiding configuration, resulting in smoother and similar changes of ΔV_H profile for AB-1.1° and AB-8.8° through the device length. As a result, the $\mathbf{p}_z$ hybridization strength introduces two different turn-on and off states to the conductance behavior in AA-devices: For lower rotation values, equivalent to high overlap between the $\mathbf{p}_z$ orbitals, the AA-devices are on their OFF state, and current is suppressed. However, for higher rotation angles, equivalent to low overlap between the $\mathbf{p}_z$ orbitals, the AA-twistronic devices are in their ON state, and an electron current is allowed to pass through the device. The conductance of AB junctions is approximately invariant to the twisting angle, and the device remains in an ON state for all values of θ.

We can quantify this in terms of the normal overlap integral of the carbon atoms in adjacent layers of AA-stacking from the following equation[32]:

$$S_{p_z}^{AA} = \frac{S_{CC}^{AA-\theta} - S_{CC}^{AB-0°}}{S_{CC}^{AA-0°} - S_{CC}^{AB-0°}}. \qquad (1)$$

In Equation (1), the term $S_{CC}^{AA-\theta} = \int \phi_{p_{zC_t}} \phi_{p_{zC_b}} d\tau$ represents the overlap integral between the atomic orbitals $\phi_{p_{zC_t}}$ and $\phi_{p_{zC_b}}$ of the carbon atoms in the top and bottom layers of the AA-stacking at the given θ values. Additionally, $S_{CC}^{AB-0°}$ denotes the overlap integral of the carbon atoms in adjacent layers of AB-stacking.

We plot the normalized overlap values in Figure 2(d). The highest value of $S_{p_z}^{AA} = 1$ is obtained for $\theta = 0°$, as expected. We note that for low twisting angles (1.1° and 2.2°), which involve a very small in-plane displacement of the top flake for the bottom layer, the $S_{p_z}^{AA}$ values show a small deviation from those of the non-twisted AA-device. A more $S_{p_z}^{AA}$ decreasing emerges by rotation for angles $\geq 4.4°$, particularly for $\theta = 8.8°$ with value of 0.543. The absolute value of 0.0012, is measured for $S_{p_z}^{AB}$ of AB-0.0° which is 5.37 times lower than AA-0.0°.

Evaluation of spin-resolved transmission spectra as a function of energy (relative to the Fermi level E_F) reveals that the conductance, especially close to E_F, gets more polarized in AA-devices (Figures (S5) SI). With this regard, the spin-current flowing through AA-1.1° and AA-8.8° twistronic devices is calculated within a bias window from −0.4 to +0.4 V. As shown in Figure 2(e), the major-spin current is higher in both systems, meaning that the twisting induces a current polarization in AA-devices. When the device's horizontal mirror symmetry breaks because of the twist of the top flake, a polarized spin-current emerges.[33]

Thermoelectric Properties of ZGNR-twistronics. To shed light on the thermoelectric properties of the investigated devices, we performed temperature-dependent charge and heat transport

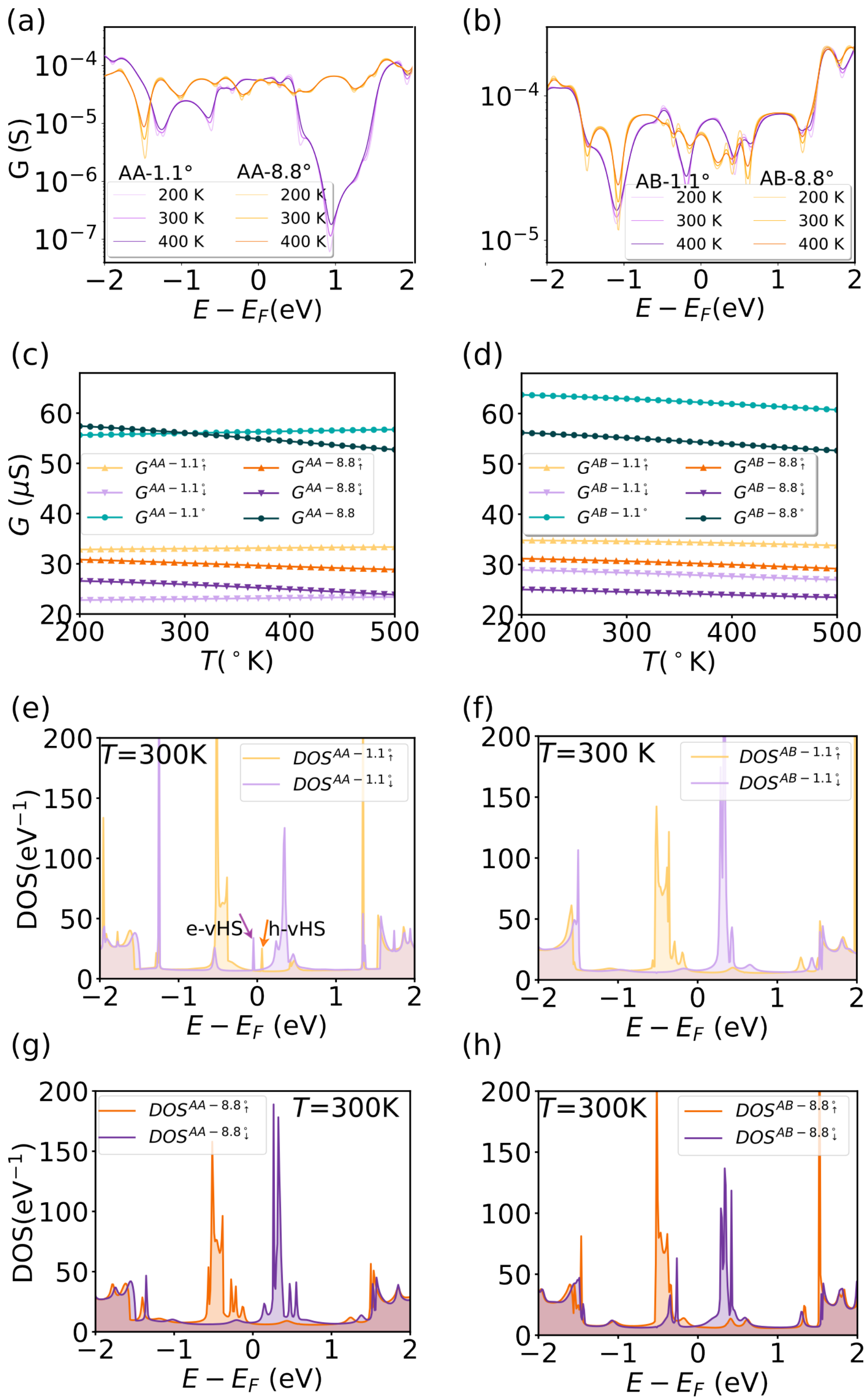

Fig. 3 Temperature influence on electron conductance, electron conductance and DOS of AA and AB-stacking devices. Semi-log plot of electrical conductance (G) of (a) AA-1.1° and AA-8.8°, (b) AB-1.1° and AB-8.8° as a function of energy ($E-E_\mathrm{F}$) at T=200, 300, and 400 K. Spin-resolved electrical conductance of (c) AA-1.1° and AA-8.8°, (d) AB-1.1° and AB-8.8° as a function temperature (T) at Fermi energy. The spin-resolved density of states (DOS) of (e) AA-1.1°, (f) AB-1.1°, (g) AA-8.8°, and (h) AB-8.8° as a function of energy ($E-E_\mathrm{F}$) at $T=300$ K. Electrical conductance, The electrical conductance, spin-resolved electrical conductance and spin-resolved density of states are obtained using DFT/PBE-D2 level of theory. The orange and purple arrows indicate the position of electron and hole vHS (e-vHS and h-vHS).

calculations for a selection of the systems analyzed above. We present in Figure 3(a)-(b) the computed electronic conductance, as a function of energy, E, at temperatures $T=200$ K, 300 K, and 400 K for θ=1.1° and 8.8° in both stacking configurations. The conductance values $G^{AA-1.1^{\circ}}_{\uparrow}$ and $G^{AA-8.8^{\circ}}_{\uparrow}$ are higher than the values $G^{AA-1.1^{\circ}}_{\downarrow}$ and $G^{AA-8.8^{\circ}}_{\downarrow}$ at all temperature gradients, indicating persistence of G spin-splitting at E_F. To explain this, we analyzed the projected density of states (DOS) at $T = 300$ K (Figure 3(e) to (h)). In all temperatures, the minor and major states are energetically delocalized. Also, at energies below E_F the number of available $\mathrm{DOS}^{AA-1.1^{\circ}}_{\uparrow}$ and $\mathrm{DOS}^{AA-8.8^{\circ}}_{\uparrow}$ are higher from than $\mathrm{DOS}^{AA-1.1^{\circ}}_{\downarrow}$ and $\mathrm{DOS}^{AA-8.8^{\circ}}_{\downarrow}$, respectively. These two factors provide not only a higher major spin conductance but also electron spin polarization.[34,35]

The comparative values of total conductance for AA and AB-devices depend on the energy values and temperature (Figure 3(c)-(d) and S7 (SI)). Here, we focus on the impact of temperature on the conductance values at $E = 0.0$, and $\pm$ 0.8 eV (Figure 3(c)-(d)) and S7 (SI) of $\theta = 1.1^{\circ}$ and 8.8° for both stacking patterns. The reason for the selected energy values ($\pm$ 0.8 eV), besides the Fermi level, is that based on our numerical simulations, the highest variations in the conductance concerning the twist angle, θ, occur at those doping levels. Overall, the spin-conductance reveals a very smooth variation with temperature. The total electrical conductance of AA-1.1° increases with temperature and at T=300 K its value becomes equal to the total electrical conductance of AA-8.8° (G=56 μS) and then its values drop under those of $G^{AA-8.8^{\circ}}$. The reason is reflected in the total DOS profile of AA-devices. The number of available states for $\theta = 1.1^{\circ}$ below and above the Fermi level demonstrates an increase with temperature and at higher temperatures there are even more states available for AA-1.1° (Figure 4(c) and (d) for total DOS). The total electrical conductance of AB-1.1° is higher than those of the AA-1.1° devices, due to higher available DOS (Figure 3(e) to (h)), while for $\theta = 8.8^{\circ}$ the G^{AA} values change very close to G^{AB}.

The temperature-dependent, spin-resolved Seebeck coefficient, S, for the selected nanodevices is plotted in Figure 4(a)-(b) and Figure S8 (SI). A positive value of the Seebeck coefficient is generally interpreted as p-type behavior, while a negative value corresponds to n-type behavior[36] In a n-type heat conductor there are more states above the E_{F} rather than below the E_{F}, whereas as in a p-type heat conductor there are a higher number of states below the E_{F} rather than above the E_{F}. Thus, for $S^{AA-1.1\uparrow}$ at $E = 0.0$ and $E = -0.8$ eV and for $S^{AB-8.8\uparrow}$ at $E = 0.0$, the p-type behavior has been observed, while n-type behavior dominates for the rest of the devices at the electrochemical potentials considered.

Based on Mott's formula,[37] the Seebeck coefficients can be expressed as

$$S = \frac{\pi^2 k_B T}{3e}\left[\frac{\partial \ln(\mathrm{DOS}(E))}{\partial E} + \frac{\partial \ln(\tau(E))}{\partial E}\right]_{E_f}, \tag{2}$$

where k_B, $\mathrm{DOS}(E)$, and $\tau(E)$ denote the Boltzmann constant, the density of states, and energy-dependent relaxation time, respectively. A large derivative of $\mathrm{DOS}(E)$ at E results in a large Seebeck coefficient. As is evident from DOS (Figure 4(c)-(d) and semi-log DOS analysis (Figure 4(g)) the number of available states for AA-1.1° is higher than the AA-8.8°, resulting in the calculated larger values of S for $S^{AA-1.1}$.

In Figure 3(e)-(h), for AA$-$1.1°, there is a higher number of $\mathrm{DOS}^{\uparrow}$ above the E_F which dominates p-type conductor behavior. Hence the $S^{AA-1.1\uparrow}$ is positive. The same reason can be used to explain positive Seebeck of $S^{AB-8.8\uparrow}$ at the Fermi level. The other junctions have both the $\mathrm{DOS}^{\uparrow}$ and $\mathrm{DOS}^{\downarrow}$ peaks below E_F (Figure 3(f)-(h)) and n-type conductor behavior directs the heat transport which is also reflected in negative values of S.

Within the studied range of temperature gradients, the values of $S^{AA-1.1}$ are higher than those of $S^{AA-8.8}$. At two extreme temperatures (T=200 and 500 K) the AA-1.1° Seebeck values are higher by factors of 5.34 to 5.96 than those of AA-8.8°. This shows the tunable electron thermal current via twisting in investigated nanodevices. Controllable heated electron transport has previously been reported for large values of twisting of bilayer graphene[38] triangulene π-dimer molecule,[39] black phosphorene bilayer,[40] with $\theta \geq 60^{\circ}$, $\geq 20^{\circ}$, and $\geq 10^{\circ}$, respectively. Now we can see the Seebeck coefficients can be tuned with larger values at very small twisting angles ($\theta \leq 10^{\circ}$) junction constructed from rectangular [6,3]-flake and nanoribbon.

The thermal conductivity is the other important parameter used to quantify the heat transport capability of a material. In our work, we treat separately the electron, κ_e, and phonon, κ_{ph}, contributions to the thermal conductivity and we neglect electron-phonon interactions.[41]. The total thermal conductivity, κ_{tot}, increases with temperature for both AA and AB-stackings, with a slightly higher value of κ_{tot} (by approximately 1 nW/K) for AB-junctions, which that arises from the higher κ_{ph} values (Figure 4(e)-(d) and Figure S9 (SI)). Similar to other carbon-based materials, thermal conductivity is dominated by phonons for all twisted devices ($\kappa_{ph} \geq \kappa_e$) for both stacking configurations.[42] An exciting result from the thermal conductivity analysis that we present in this article is the fact that the electron thermal conductivity of low-twisting devices is larger than that of higher-twisting angle devices in both AA and AB configurations at the Fermi level (E_F), and this effect is more pronounced for the AA-1.1° device. The change in the heat transport capability of AA and AB-devices (Figure 3 (b) and (c)) can be better understood by analyzing the semi-log plot of the DOS at different temperature gradients (T = 200 K, 300 K, 400 K). Evaluation of the DOS not only demonstrates that a higher number of states is available close to E_{F} for low twisted devices in both stacking configurations, but also the coexistence of two distinct van Hove singularity (vHS) flavors near the Fermi level of AA-1.1°; electron-vHS and hole-vHS (Figure 4(g)). Interlayer orbital overlapping ensures electron hopping between neighboring graphene layers and the emergence of two saddle points in the band structure (pink and purple arrows in Figure 1(f)) due to the overlaid Dirac cones[43] giving rise to logarithmic vHS in the DOS profile (circled area in Figure 4(g)). The vHS was observed in twisted silicene multilayers,[43] twisted monolayer–bilayer graphene,[44] kagome metal $\mathrm{CsV_3Sb_5}$,[45] *etc*. When the vHS is located sufficiently close to the Fermi level, its magnified DOS causes electronic instability, hence resulting in new phases of matter with special properties, such as superconductivity, magnetism, and density waves.[46] On the other hand, such electron and hole-vHSs appear on both the electron and hole sides of AA-1.1° and are highly tunable with varying temperature (Figure 4(g)), which can make them acces-

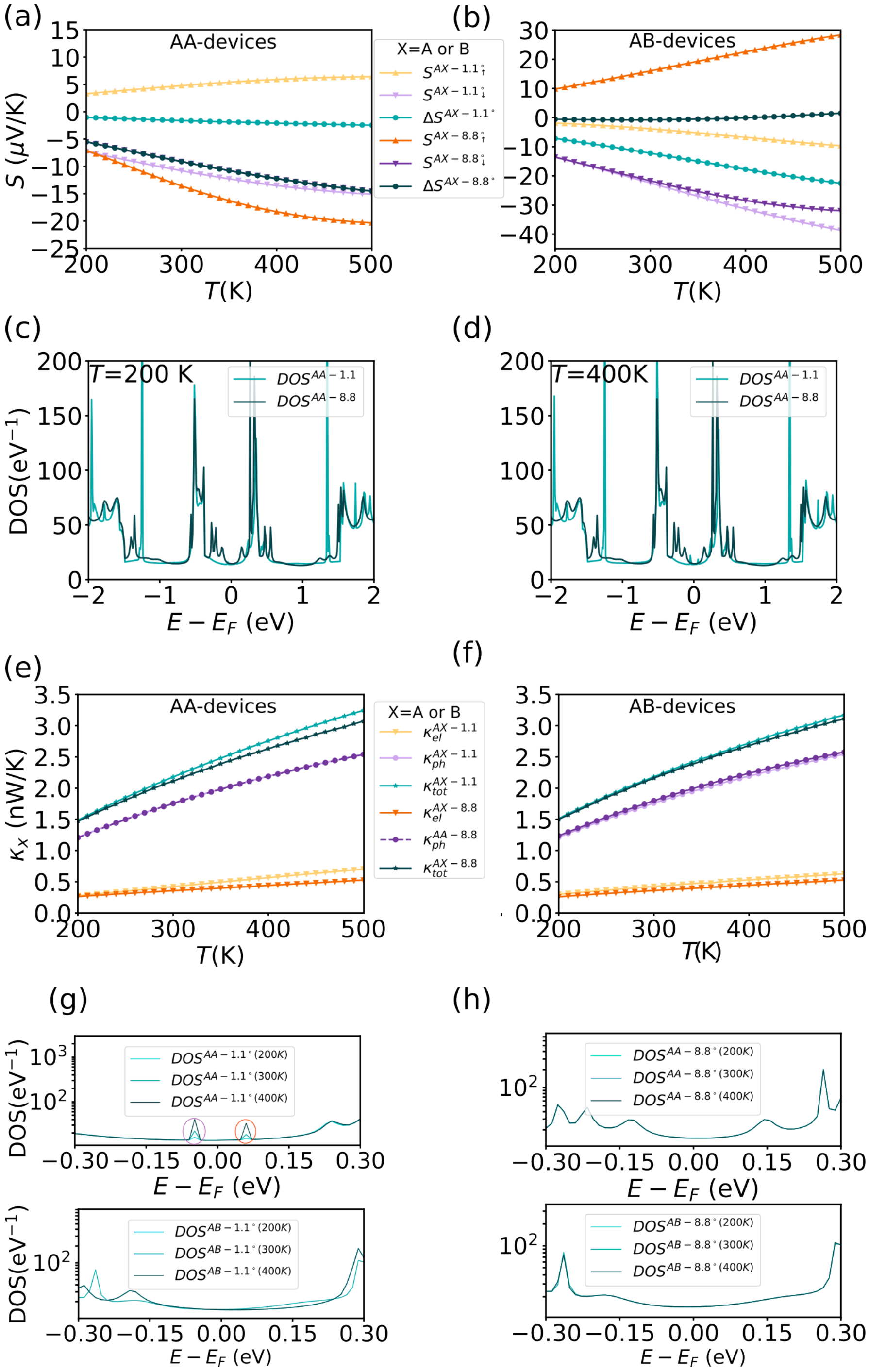

Fig. 4 Heat transport properties and temperature-dependence of DOS in AA and AB-stacking devices Spin-resolved Seebeck coefficient (S) of (a) AA-1.1° and AA-8.8°, (b) AB-1.1° and AB-8.8° as a function of temperature (T) at Fermi energy (E_F). The DFT-calculated density of states (DOS) for AA-1.1° and AA-8.8° at (c) $T = 200$ K and (d) $T = 400$ K. Electron (κ_e), phonon (κ_{ph}) , and total (κ_{tot}) thermal conductivity of (e) AA-1.1° and AA-8.8°, (f) AB-1.1° and AB-8.8° as a function of temperature (T) at Fermi energy (E_F). The semi-log plot of the density of states (DOS) at around Fermi energy at $T = 200$, 300, 400 K for (g) AA-1.1° and AA-8.8° and (h) AB-1.1° and AB-8.8°. The purple and orange circles show the conservation of hole and electron-vHS in a semi-log DOS plot with temperature increasing which results in enhanced κ_{tot} of this device. The spin-resolved Seebeck coefficient, thermal conductivity and the density of states are obtained using DFT/PBE-D2 level of theory.

sible in experiments.[44] It should be pointed out that the electronic structure calculations can show artificial peaks in a DOS profile that do not arise from a vHS. However, we believe that, as the signature of both electron-vHS and hole-vHS is maintained in the various studies described in our investigation, they do not seem to be a numerical artifact. For example, the spin-polarized band structure of the central part of AA-1.1° (Figure 1(f)) exhibits flatness of CB$^\uparrow$ (pink band, marked by pink arrow) and VB$^\downarrow$ (blue band, marked by blue arrow) which features hole-vHS (for majority spin) and electron-vHS (for minority spin) in the spin-polarized DOS profile in Figure 3(e) (light orange peak for hole-vHS and light purple peak for electron-vHS) and also logarithmic spin-off DOS profile in Figure 4(g). Both DOS and spin-DOS are computed using DFT/PBE+D2, where the temperature is set to 300 K. The footprint of electron-vHS and hole-vHS was identified in our quantum transport simulations using the NEGF/DRSLL approach mentioned above (Figure S5(c) (SI)). Naturally, further experimental studies can shed more light on the significance and features of such temperature-stable electron and hole-vHS.

In our future studies, we plan to focus on the same system but with a different category of materials based on transition metal dichalcogenides (TMD). This will enable us to investigate how the material class could alter the scenario for both electron and heat transport properties. Additionally, we will explore scenarios where the nanoflake's shape deviates from the rectangular benzenoid, potentially impacting the electronic and transport properties of the device in unique ways.

Feasible experimental fabrication methods: Both components of nanodevices proposed in this work, rectangular benzenoid [6,3]-flake and 6-ZGNR, can be experimentally fabricated. Utilizing on-surface synthesis techniques under ultrahigh vacuum conditions, researchers can fabricate atomically precise carbon flakes, enabling unprecedented control over their structural and electronic properties .[47]Desired type of GNRs can be also synthesised from small molecules through bottom-up approaches which allow for full control of their widths and edge structures.[48] The main challenge in the experimental realization of proposed nanodevices is the precise control over the twisting angle while performing thermoelectric measurements of the proposed devices. Seebeck's coefficient of near-magic angle twisted bilayer graphene nanodevices was already experimentally measured[49]. Although it was done in the static configuration which does not allow tuning the twisting angle. In other experimental works of twisted 2D systems[23,29,50,51] it was demonstrated that dynamical tuning of twisting angle is possible and usually performed using atomic force microscopy (AFM) or scanning tunneling microscope (STM) tip. However, experimental setups in those experiments do not allow to measure easily neither Seebeck coefficient nor thermal conductance as they provide good thermal and/or electrical contact between bottom layer and the substrate. To overcome this limitation and facilitate the measurement of thermoelectric properties, we propose to use suspended nanoribbon. Nanoribbon can be fabricated on or transferred to substrate placed on a rotating table. Substrate below the nanoribbon can be removed by etching[52] or other methods after fabrication or before transfer, making it freestanding, as is the case considered in this study. Manipulating the nanoribbon's position while keeping the flake's position constant offers several advantages. Firstly, it allows for precise control over both the flake-nanoribbon angle and the forces applied between them. This precision is essential for achieving accurate and reproducible experimental results. Secondly, using STM tip(s) located on the flake to change the angle between the flake and the suspended nanoribbon increases the risk of unintentional removal of the flake from the nanoribbon during the rotation. Therefore, we propose to pin the flake on a particular position by a scanning tunneling microscope (STM) tips.[23] Using multi-tip STM[53] could not only be an efficient method that can help to fix the flake but also could allow precise control of the temperature thus enabling thermoelectric measurements. Tips should be placed as follows: one tip on the left end of the nanoribbon (left electrode), two on the flake, and one tip on the right end of the nanoribbon (right electrode). The left electrode of ZGNR and top flake would have the same temperature and be treated as cold leads. A laser pulse can be applied to the last tip to increase its temperature to the desired level (hot lead) for thermoelectric measurements.

Simulation methods: Density functional theory (DFT) calculations were performed based on the Dion, Rydberg, Schröder, Langreth, and Lundqvist[54] (DRSLL) vdW-DF exchange-correlation functional as implemented in `SIESTA` suite of programs[55] and Perdew-Burke-Ernzerhof (PBE)[56] parameterization of the exchange-correlation functional in `QuantumATK`, as vdW functionals are not still implemented in this code.[57–59] The dispersion interactions between nanoribbon and flake in QuantumATK calculations (PBE) were included in the total bonding energy using the methodology proposed by Grimme.[60] The core electrons were described by non-conserving Troullier-Martins pseudopotentials[61] and a double-ζ plus polarization (DZP) basis set for the valence-electron wave functions.

First, we relaxed the 6-ZGNR unit cell with a force tolerance of 10^{-3} eV/Ang. The relaxed structure was replicated 16 times to build the bottom layer. The relaxed top rectangular benzenoids [6,3]-flake was placed at a distance of 3.34 Å (3.17 Å) and 3.22 Å (3.12 Å) above the ZGNR, which are the distances at which the calculated energy was lowest for AA and AB-stackings using DRSLL (PBE+D2) in our simulations. In this study, we focus on a low-twisting angle of the ZGNR bilayer where $1.1^\circ \leq \theta \leq 8.8^\circ$. We performed the band structure analysis over the central region without electrodes. In this context, the bottom layer can be conceptualized as an infinite, periodically decorated zigzag graphene nanoribbon (ZGNR) with the top nanoflake. The spin-dependent conductance phenomena of all nanodevices are calculated with the NEGF formalism as implemented in `TranSIESTA`[62] and `QuantumATK`[58,63] codes. To keep a balance between the time and accuracy of computation we use the DZ basis set for simulations of coherent electron transport. The electrode structures and the determination method[64,65] for the lattice parameter are presented in Figure S10 (SI). Electrodes are made of three 6-ZGNR unit cells and for their calculations, 75 k-points were used along the periodic direction (z-axis). A level broadening of $\eta = 10^{-6}$ eV is considered in the electrode simulations. The thermoelectric properties in the ballistic transport limit, including the dependence of the electrical conductance, G, Seebeck's coefficient, S, and electron thermal conductance, κ_e on temperature, T ranging from 200 K to 500 K were calculated using linear response theory.[58,66] The thermoelectric calculations were performed in the `QuantumATK` using a DFT/PBE+D2/DZ approach for the electronic contribution and reactive force field[67] for the phonon contribution. The convergence parameters were chosen as in the `SIESTA` calculations above. A comparison between the obtained transmission coefficients ($\overline{T}$) results obtained using `TranSIESTA` and `QuantumATK` for the AA-1.1° device is shown in Figure S11

(SI). The overall obtained transmission characteristic using both codes shows that except for the values at around E_F, the calculated $\overline{T}$ using the DRSLL approach is higher by the value of 0.30 G_0 at the Fermi level but in good agreement with those obtained using the PBE+D2 exchange-correlation functional (Note S13 (SI)). A similar optimization procedure was also used to obtain the phonon transmission in the reactive force field approach. The dynamical matrices of all device systems were calculated using the finite difference method in a repeated cell (frozen phonon method). The maximum force tolerance was set at 10^{-11} Ha/Bohr^2, and the distance by which the atoms are displaced was equal to 0.001 Å. The phonon transmission spectra were calculated in the range of (0, 0.5) eV, using 501 sample points between 0 and 0.5. Details of the thermoelectric simulations can be found in Note S14 (SI).[57–59,68,69]

3 Conclusions

We have demonstrated, using first-principles calculations, that the electronic and thermoelectric properties in nanodevices composed of a twisted [6,3] rectangular flake and a ZGNR are highly tunable. Our studies reveal that a twisting angle $0^\circ \leq \theta \leq 8.8^\circ$, depending on the stacking configuration, can influence both the charge and heat transport capability of the considered devices. Twisting of the top flake switches the charge carrier's conductance from an OFF-state (for $\theta \leq 2.2^\circ$) to an ON-state (for $\theta \geq 4.4^\circ$) in AA-stacking nanodevices. This feature can be used to control and manage the flow of electricity in nanodevices. In contrast, such twist-driven switching characteristic has not been observed in AB-stacking nanodevices.

We also observed the hole and electron-vHS very close to the Fermi level of AA-1.1° junction as a result of strong interlayer coupling when the top flake is rotated by a minimal angle. These vHSs are formed as a result of the flatness of CB$^{\downarrow}$ and VB$^{\uparrow}$ and their signature is reflected in the band structure, DOS, and electron conductance spectral analysis. The vHSs are persistent with temperature and hence, impact the temperature-dependent phenomena in the designed devices. As a result, the induced thermoelectric voltage (Seebeck coefficient) in the AA-1.1° device was found to be higher than that of the AA-8.8° device and also AB-1.1°. The AA-1.1° also shows larger values of κ_e and the total thermal conductivity in comparison with AA-8.8° and AB-devices, which shows the possibility of tuning the thermal properties with twisting. This could extend the applications of twistronics from electronics to thermoelectric. Our findings particularly offer opportunities for further exploration, engineering, and construction of exciting new nanodevices with more controllable topological, electronic, and thermal properties, such as electronic nanoswitches,[70] higher temperature superconductors,[71] etc.

Author contributions

Azar Ostovan: Conceptualization, Investigation, Methodology, Data curation, Formal analysis, Writing–Original draft, Visualization. **Karolina Z. Milowska:** Investigation, Methodology, Formal analysis, Resources, Writing–Review & Editing, Visualization. **Carlos J. García-Cervera:** Supervision, Resources, Funding acquisition, Formal analysis, Writing–Review & Editing.

All authors contributed to the interpretation of results and approved the final version of the manuscript.

Conflicts of interest

The authors declare no competing interests.

Acknowledgements

The work of CJGC and AO was supported by the Air Force Office of Scientific Research under award number FAA9550-18-1-0095. CJGC and AO also acknowledge support from the Center for Scientific Computing at the CNSI and MRL: an NSF MRSEC (DMR-1121053) and NSF CNS-0960316. KZM gratefully acknowledges the Interdisciplinary Centre for Mathematical and Computational Modeling at the University of Warsaw (Grant No. G47-5) for providing computer facilities. We also would like to thank Sohini Kar-Narayan, Fabian Schulz and José I. Pascual for the discussion on the possible experimental realization of our systems.

Notes and references

1 Y. Cao, V. Fatemi, S. Fang, K. Watanabe, T. Taniguchi, E. Kaxiras and P. Jarillo-Herrero, *Nature*, 2018, **556**, 43–50.

2 S. Dai and Q. Ma, *Nat. Mater.*, 2023, **22**, 1–2.

3 J. Li, Y.-M. Niquet and C. Delerue, *Phys. Rev. B*, 2023, **107**, 245417.

4 A. Y. Nikitin, *Nat. Nanotechnol.*, 2021, **16**, 489–490.

5 H. C. Po, L. Zou, A. Vishwanath and T. Senthil, *Phys. Rev. X.*, 2018, **8**, 031089.

6 M. Yankowitz, S. Chen, H. Polshyn, Y. Zhang, K. Watanabe, T. Taniguchi, D. Graf, A. F. Young and C. R. Dean, *Science*, 2019, **363**, 1059–1064.

7 H. Chi and J. S. Moodera, *APL Materials*, 2022, **10**, 090903.

8 S. Carr, D. Massatt, M. Luskin and E. Kaxiras, *Phys. Rev. Res.*, 2020, **2**, 033162.

9 E. Y. Andrei and A. H. MacDonald, *Nat. Mater.*, 2020, **19**, 1265–1275.

10 L. Du, T. Hasan, A. Castellanos-Gomez, G.-B. Liu, Y. Yao, C. N. Lau and Z. Sun, *Nat. Rev. Phys.*, 2021, **3**, 193–206.

11 V. V. Enaldiev, F. Ferreira and V. I. Fal'ko, *Nano Lett.*, 2022, **22**, 1534–1540.

12 H. Zhu, J. Yi, M.-Y. Li, J. Xiao, L. Zhang, C.-W. Yang, R. A. Kaindl, L.-J. Li, Y. Wang and X. Zhang, *Science*, 2018, **359**, 579–582.

13 J. L. Lado, *Science*, 2021, **374**, 1048–1049.

14 Y. S. Gani, E. J. Walter and E. Rossi, *Phys. Rev. B*, 2020, **101**, 195416.

15 N. Suri, C. Wang, Y. Zhang and D. Xiao, *Nano Lett.*, 2021, **21**, 10026–10031.

16 P. Brandimarte, M. Engelund, N. Papior, A. Garcia-Lekue, T. Frederiksen and D. Sánchez-Portal, *J. Chem. Phys.*, 2017, **146**, 092318.

17 S. Sanz, P. Brandimarte, G. Giedke, D. Sánchez-Portal and T. Frederiksen, *Phys. Rev. B*, 2020, **102**, 035436.

18 S. Sanz, N. Papior, G. Giedke, D. Sánchez-Portal, M. Brandbyge and T. Frederiksen, *Phys. Rev. Lett.*, 2022, **129**, 037701.

19 J. R. Dias, *J. Phys. Chem. A*, 2013, **117**, 4716–4725.

20 H. Nagai, M. Nakano, K. Yoneda, R. Kishi, H. Takahashi, A. Shimizu, T. Kubo, K. Kamada, K. Ohta, E. Botek *et al.*, *Chem. Phys. Lett.*, 2010, **489**, 212–218.

21 M. Birowska, K. Milowska and J. Majewski, *Acta Phys. Pol.*, 2011, **120**, 845–848.

22 Z. Liu, K. Suenaga, P. J. Harris and S. Iijima, *Phys. Rev. Lett.*, 2009, **102**, 015501.

23 D. Wang, D.-L. Bao, Q. Zheng, C.-T. Wang, S. Wang, P. Fan, S. Mishra, L. Tao, Y. Xiao, L. Huang *et al.*, *Nat. Commun.*, 2023, **14**, 1018.

24 S. Pathak, T. Rakib, R. Hou, A. Nevidomskyy, E. Ertekin, H. T. Johnson and L. K. Wagner, *Phys. Rev. B*, 2022, **105**, 115141.

25 S. Lisi, X. Lu, T. Benschop, T. A. de Jong, P. Stepanov, J. R. Duran, F. Margot, I. Cucchi, E. Cappelli, A. Hunter *et al.*, *Nat. Phys.*, 2021, **17**, 189–193.

26 S. Simdyankin, S. Elliott, Z. Hajnal, T. A. Niehaus and T. Frauenheim, *Phys. Rev. B*, 2004, **69**, 144202.

27 S. Wang, C. Qin, W. Liu, B. Wang, F. Zhou, H. Ye, L. Zhao, J. Dong, X. Zhang, S. Longhi *et al.*, *Nat. Commun.*, 2022, **13**, 7653.

28 W. A. Muñoz, S. K. Singh, J. F. Franco-González, M. Linares, X. Crispin and I. Zozoulenko, *Phys. Rev. B*, 2016, **94**, 205202.

29 E. Koren, I. Leven, E. Lörtscher, A. Knoll, O. Hod and U. Duerig, *Nat. Nanotechnol.*, 2016, **11**, 752–757.

30 S. Zhang, A. Song, L. Chen, C. Jiang, C. Chen, L. Gao, Y. Hou, L. Liu, T. Ma, H. Wang *et al.*, *Sci. Adv.*, 2020, **6**, eabc5555.

31 T. Frederiksen, M. Paulsson, M. Brandbyge and A.-P. Jauho, *Phys. Rev. B*, 2007, **75**, 205413.

32 O. Hod, *Phys. Rev. B*, 2012, **86**, 075444.

33 C. M. Acosta and A. Fazzio, *Phys. Rev. Lett.*, 2019, **122**, 036401.

34 R. E. Blackwell, F. Zhao, E. Brooks, J. Zhu, I. Piskun, S. Wang, A. Delgado, Y.-L. Lee, S. G. Louie and F. R. Fischer, *Nature*, 2021, **600**, 647–652.

35 M. Pizzochero and E. Kaxiras, *Nano Lett.*, 2022, **22**, 1922–1928.

36 B. Kumanek, K. Z. Milowska, Ł. Przypis, G. Stando, K. Matuszek, D. MacFarlane, M. C. Payne and D. Janas, *ACS Appl. Mater. Interfaces*, 2022, **14**, 25861–25877.

37 M. Cutler and N. F. Mott, *Phys. Rev.*, 1969, **181**, 1336–1340.

38 P. S. Mahapatra, B. Ghawri, M. Garg, S. Mandal, K. Watanabe, T. Taniguchi, M. Jain, S. Mukerjee and A. Ghosh, *Phys. Rev. Lett.*, 2020, **125**, 226802.

39 D. Wu, L. Huang, P.-Z. Jia, X.-H. Cao, Z.-Q. Fan, W.-X. Zhou and K.-Q. Chen, *Appl. Phys. Lett.*, 2021, **119**, 063503.

40 S. Duan, Y. Cui, W. Yi, X. Chen, B. Yang and X. Liu, *Small*, 2022, **18**, 2204197.

41 Q. Li, F. Liu, S. Hu, H. Song, S. Yang, H. Jiang, T. Wang, Y. K. Koh, C. Zhao, F. Kang *et al.*, *Nat. Commun.*, 2022, **13**, 4901.

42 A. A. Balandin, *Nat. Mater.*, 2011, **10**, 569–581.

43 Z. Li, J. Zhuang, L. Chen, Z. Ni, C. Liu, L. Wang, X. Xu, J. Wang, X. Pi, X. Wang *et al.*, *ACS Cent. Sci.*, 2016, **2**, 517–521.

44 S. Xu, M. M. Al Ezzi, N. Balakrishnan, A. Garcia-Ruiz, B. Tsim, C. Mullan, J. Barrier, N. Xin, B. A. Piot, T. Taniguchi *et al.*, *Nat. Phys.*, 2021, **17**, 619–626.

45 Y. Hu, X. Wu, B. R. Ortiz, S. Ju, X. Han, J. Ma, N. C. Plumb, M. Radovic, R. Thomale, S. D. Wilson *et al.*, *Nat. Commun.*, 2022, **13**, 2220.

46 G. Li, A. Luican, J. Lopes dos Santos, A. Castro Neto, A. Reina, J. Kong and E. Andrei, *Nat. Phys.*, 2010, **6**, 109–113.

47 S. Mishra, T. G. Lohr, C. A. Pignedoli, J. Liu, R. Berger, J. I. Urgel, K. Müllen, X. Feng, P. Ruffieux and R. Fasel, *ACS Nano*, 2018, **12**, 11917–11927.

48 H. Wang, H. S. Wang, C. Ma, L. Chen, C. Jiang, C. Chen, X. Xie, A.-P. Li and X. Wang, *Nat. Rev. Phys.*, 2021, **3**, 791–802.

49 B. Ghawri, P. S. Mahapatra, M. Garg, S. Mandal, S. Bhowmik, A. Jayaraman, R. Soni, K. Watanabe, T. Taniguchi, H. R. Krishnamurthy, M. Jain, S. Banerjee, C. U. and A. Ghosh, *Nat. Comm.*, 2022, **13**, 1522.

50 N. C. H. Hesp, I. Torre, D. Barcons-Ruiz, H. Herzig Sheinfux, K. Watanabe, T. Taniguchi, R. Krishna Kumar and F. H. L. Koppens, *Nat. Comm.*, 2021, **12**, 1640.

51 K. Yao, N. R. Finney, J. Zhang, S. L. Moore, L. Xian, N. Tancogne-Dejean, F. Liu, J. Ardelean, X. Xu, D. Halbertal, K. Watanabe, T. Taniguchi, H. Ochoa, A. Asenjo-Garcia, X. Zhu, D. N. Basov, A. Rubio, C. R. Dean, J. Hone and P. J. Schuck, *Sci. Adv*, 2021, **7**, eabe8691.

52 T. He, Z. Wang, F. Zhong, H. Fang, P. Wang and W. Hu, *Adv. Mater. Technol.*, 2019, **4**, 1900064.

53 A. Leis, V. Cherepanov, B. Voigtländer and F. S. Tautz, *Rev. Sci. Instrum.*, 2022, **93**, 013702.

54 M. Dion, H. Rydberg, E. Schröder, D. C. Langreth and B. I. Lundqvist, *Phys. Rev. Lett.*, 2004, **92**, 246401.

55 J. M. Soler, E. Artacho, J. D. Gale, A. García, J. Junquera, P. Ordejón and D. Sánchez-Portal, *J. Condens. Matter Phys.*, 2002, **14**, 2745.

56 J. P. Perdew, K. Burke and M. Ernzerhof, *Phys. Rev. Lett.*, 1996, **77**, 3865.

57 *Synopsys QuantumATK Version 2022.03-SP1 (accessed 11-07-2023)*, `https://www.synopsys.com/silicon/quantumatk.html`.

58 K. Stokbro, D. Petersen, S. Smidstrup, A. Blom, M. Ipsen and K. Kaasbjerg, *J. Condens. Matter Phys.*, 2020, **32**, 015901.

59 K. Stokbro, D. Petersen, S. Smidstrup, A. Blom, M. Ipsen and K. Kaasbjerg, *Phys. Rev. B*, 2010, **82**, 075420.

60 S. Grimme, *J. Comput. Chem.*, 2006, **27**, 1787–1799.

61 N. Troullier and J. Martins, *Solid State Commun.*, 1990, **74**, 613–616.

62 N. Papior, N. Lorente, T. Frederiksen, A. García and M. Brandbyge, *Comput. Phys. Commun.*, 2017, **212**, 8–24.

63 M. Brandbyge, J.-L. Mozos, P. Ordejón, J. Taylor and K. Stokbro, *Phys. Rev. B*, 2002, **65**, 165401.

64 A. Ostovan, Z. Mahdavifar and M. Bamdad, *J. Mol. Liq.*, 2018, **269**, 639–649.

65 A. Ostovan, N. Papior and S. S. Naghavi, *Phys. Rev. B*, 2021,

104, 235435.

66 J.-W. Jiang, J.-S. Wang and B. Li, *J. Appl. Phys.*, 2011, **109**, 014326.

67 Q. Mao, Y. Ren, K. Luo and A. C. D. van Duin, *J. Chem. Phys.*, 2017, **147**, 244305.

68 S. Datta, *Electronic Transport in Mesoscopic Systems*, Cambridge University Press, 1997.

69 N. W. Ashcroft and N. D. Mermin, *Solid State Physics*, New York: Saunders College Publishing, 1976.

70 A. M. Ionescu and H. Riel, *Nature*, 2011, **479**, 329–337.

71 T.-T. Gai, P.-J. Guo, H.-C. Yang, Y. Gao, M. Gao and Z.-Y. Lu, *Phys. Rev. B*, 2022, **105**, 224514.